Journal Pre-proof

Constrained titanohematite formation at BTO/Fe interfaces deposited by RF-sputtering

C.O. Amorim, K. Sloyan, M.R. Correia, A.A.C.S. Lourenço, M.S. Dahlem, Vítor S. Amaral

PII: S0925-8388(20)30607-1

DOI: https://doi.org/10.1016/j.jallcom.2020.154244

Reference: JALCOM 154244

To appear in: *Journal of Alloys and Compounds*

Received Date: 4 November 2019

Revised Date: 27 January 2020

Accepted Date: 8 February 2020

Please cite this article as: C.O. Amorim, K. Sloyan, M.R. Correia, A.A.C.S. Lourenço, M.S. Dahlem, Ví.S. Amaral, Constrained titanohematite formation at BTO/Fe interfaces deposited by RF-sputtering, *Journal of Alloys and Compounds* (2020), doi: https://doi.org/10.1016/j.jallcom.2020.154244.

C. O. Amorim: Conceptualization, Methodology, Validation, Investigation, Writing - Original Draft

K. Sloyan: Validation, Investigation, Resources, Writing - Review & Editing

M. R. Correia: Validation, Investigation, Resources

A. A. C. S. Lourenço: Conceptualization, Validation, Resources

M. S. Dahlem: Validation, Resources, Writing - Review & Editing, Supervision, Project administration,

Vítor S. Amaral: Conceptualization, Methodology, Writing - Review & Editing, Supervision, Project administration, Funding acquisition

Constrained titanohematite formation at BTO/Fe interfaces deposited by RF-sputtering

C. O. Amorim[a], K. Sloyan[b], M. R. Correia[c], A. A. C. S. Lourenço[a], M. S. Dahlem[d], Vítor S. Amaral[a]

[a]Physics Department and CICECO, University of Aveiro, 3810-193 Aveiro, Portugal

[b]Department of Electrical and Computer Engineering, Khalifa University of Science and Technology, Abu Dhabi, United Arab Emirates

[c]Physics Department and I3N, University of Aveiro, 3810-193 Aveiro, Portugal

[d]Interuniversity Microelectronics Center (IMEC), Kapeldreef 75, 3001 Leuven, Belgium

Email address: amorim5@ua.pt (C. O. Amorim)

Abstract

The usage of heterostructures of ferromagnetic and ferroelectric materials, as a means of achieving magnetoelectric multiferroic coupling, is a widely used approach which has been showing promising results. Following this line of thought, the deposition of $BaTiO_3$ and Fe multilayers on $LaAlO_3$, MgO, Al_2O_3 and $SrTiO_3$ substrates using RF-magnetron sputtering was carried out to study its viability to produce magnetoelectric heterostructures.

It is shown that each substrate constrains the growth of the deposited thin films, even for the same deposition conditions. This is clearly seen through the magnetic properties of the thin film, mainly after performing a 900°C thermal annealing on air. The thermal annealing results in the creation of iron oxides specific of each one of the substrates where the deposition took place.

Keywords: Titanohematite, Magnetoelectric coupling, Multiferroics, Interfaces, RF-sputtering

1. Introduction

Multiferroic magnetoelectric materials present coupled magnetic and electric ordering [1-4]. Such a coupling is very interesting due to the multiple technological applications, such as their usage in electronic devices, memories, sensors, energy harvesting and many others [5-11].

This type of materials has been taking part of the material and physics research during the last decade. Intrinsic magnetoelectric materials are quite rare and/or non-competitive due to the apparent incompatibility of the magnetic and electric order prerequisites [12]. On the other hand, extrinsic magnetoelectric materials possess two or more phases of electrically and/or magnetically ordered materials which couple through some kind of mechanism (usually via a strain mediated effects) and currently present the most efficient and versatile approach for the synthesis of a competitive magnetoelectric material [4, 6, 13-15].

Heterostructures containing $BaTiO_3$ (BTO) and/or Fe phases have been widely studied since these materials are individually competitive, non-critic and inexpensive ferroelectric and ferromagnetic materials, respectively. These heterostructures can present several magnetoelectric effects depending on the interfaces and conditions assumed/used in the reported studies, thus it is expectable that the synthesis conditions and/or substrates can be used as a means of tuning the electric, magnetic and magnetoelectric properties of these heterostructures [10, 16-22].

In this manuscript, we studied BTO/Fe heterostructures deposited on $LaAlO_3$, MgO, Al_2O_3 and $SrTiO_3$ substrates, using magnetron sputtering. We investigated the influence of the substrate on the growth conditions of the ferroic phases, as well as how these phases behave after thermal treatments, with a detailed structural and magnetic study.

2. Experimental Details

The BTO/Fe heterostructures consisted of multi-layers of BTO and Fe deposited simultaneously on top of four substrates - $LaAlO_3$(100), MgO(100), Al_2O_3(0001) and $SrTiO_3$(100) - using RF magnetron sputtering. The deposition conditions are presented in table 1. For $BaTiO_3$ deposition, a 99.9% purity target from Kurt J. Lesker was used, while for the Fe deposition, a Fe foil was used as a target [23]. All the substrates were provided by CrysTec GmbH [24].

The geometry of the deposited thin films consisted of a 7-layer heterostructure (4 BTO layers and 3 Fe layers), with a total thickness of ≈ 72 nm, as illustrated in figure 1. The thickness of

each single layer presented in figure 1 was measured by Scanning Transmission Electron Microscopy (STEM) and Energy-dispersive X-ray spectroscopy (EDS), as it will be shown later.

Table 1: Table 1: RF-Sputtering conditions for each layer. P_{dep} is the sputtering deposition power, D[T-S] is the distance between the target and the substrate, P_{total} is the total pressure inside the deposition chamber, O_2/Ar is the partial pressure percentage of the O_2, and T_{sub} is the temperature of the substrate.

Layer	P_{dep} (W)	D[T-S] (mm)	P_{total} (mbar)	O_2/Ar (%)	T_{sub} (°C)
$BaTiO_3$	50	125	1.0×10^{-2}	7	350
Fe	14	125	1.2×10^{-2}	0	350

The films were studied before and after annealings at different temperatures in air. The thermal annealing temperatures (600°C and 900°C) were chosen to be close to the Fe diffusion temperature in $SrTiO_3$ (800°C), a close relative of $BaTiO_3$, based on emission channeling and hyperfine technique studies [25]. The annealing temperatures and durations are presented in table 2. After the annealing process, the samples were cooled down in air. For two samples, an additional higher temperature annealing was carried out. The total annealing duration does not include the time required to achieve the annealing temperature (achieved by a heating ramp of ≈ 10°C/minute).

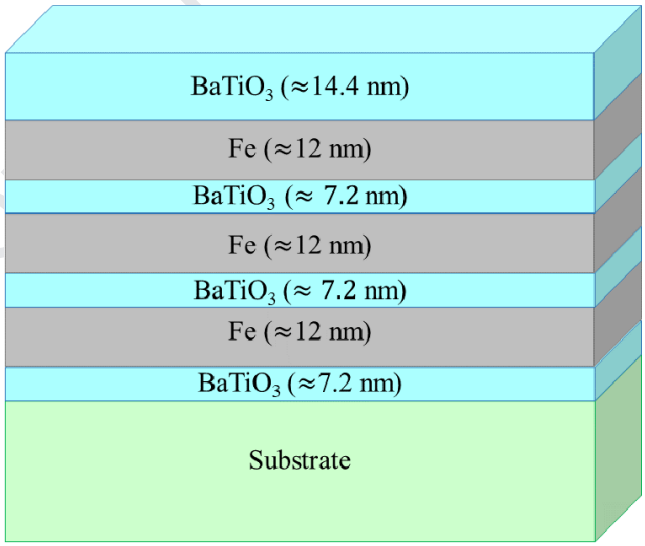

Figure 1: Illustration of the seven layer heterostructure deposited by RF-Sputtering.

X-Ray Diffraction (XRD) measurements were performed adopting a grazing incidence geometry (1° incidence angle), in a *Philips Panalytical X'Pert Pro MRD* using λ (Cu $K_{\alpha 1}$)=1.5405(98)Å (without monochromator) at room temperature. The High Score Plus phase indexing software, which uses the *ICDD PDF4+* as database reference, was used for a preliminary identification of the crystalline phases of each sample.

Table 2: Thermal annealing details for each sample.

	1st Annealing		2nd Annealing	
Sample	**t (h)**	**T (°C)**	**t (h)**	**T (°C)**
BTO/Fe $LaAlO_3$	24	600	24	900
BTO/Fe MgO	24	600	24	900
BTO/Fe $Al2O_3$	48	900	-	-
BTO/Fe $SrTiO_3$	48	900	-	-

Raman spectroscopy measurements were performed at room temperature in the range 100-2000 cm^{-1}, using a *Jobin-Yvon LabRaman HR 800* spectrometer equipped with a multichannel air cooled (253 K) CCD detector and an *Olympus BX41* microscope. A HeCd laser line of 442nm was used as excitation source and the Raman signal acquisition was performed in the backscattering configuration.

STEM images and EDS results were obtained by a *FEI Tecnai G2* (200 kV) equipped with an EDAX EDS detector. A *FEI Helios NanoLab* 650 FIB/SEM dual-beam system was used for TEM specimen preparation. To dissipate the charges built-up on the sample surface during the ion beam milling, the specimen was first sputter coated with a thin layer of Al. An additional Pt layer was deposited by an ion beam, followed by an electron beam to protect the sample surface layer.

Magnetic measurements were performed using a *Quantum Design* MPMS3 SQUID-VSM in the 2-400K temperature range and using magnetic fields ranging from -70 kOe-70 kOe.

3. Results and Discussion

3.1. Grazing Incidence XRD

Given that we are dealing with very thin films deposited at low temperatures, a low level of crystallinity is expected, at least for the "as deposited" samples, mainly for the BTO layers. To avoid the masking of results by the substrate diffraction peaks, a grazing incidence (GI) geometry was adopted to increase the interaction volume of the X-ray radiation with the thin films and reduce the contribution from the substrate. Figure 2 shows the diffractograms obtained from the deposited thin films, with and without the final thermal treatments.

The diffractogram of each sample presents a scarce number of diffraction peaks (if any), thus making the phase identification/indexation quite hard/ambiguous. Nonetheless, even though all the samples have the same deposition conditions, it is possible to see that the main diffraction peaks differ from substrate to substrate, even for the same annealing temperatures, implying that the substrates constrain the crystallization process of the thin films.

The lack of reliable diffraction peaks might be related to the very small thickness of each deposited layer, which influences the size of BTO grains (thicker layers will have bigger grains) [26]. Nevertheless, taking into account the deposited elements and the suggestions from the indexing software, we can have some hints about which possible phases can be assigned to the peaks displayed in the diffractograms.

The GIXRD results for the thin films deposited on the $LaAlO_3$ substrate show that there are almost no diffraction peaks, apart from one at around $2\theta = 61°$. This diffraction plane is not indexed to any of the most intense powder diffraction peaks of Fe, Fe oxides or barium titanate phases. It can however be assigned to some lower intensity peaks of less common barium titanate compounds (Ba_2TiO_4, $BaTi_2O_5$ and $BaTi_5O_{11}$), suggesting a possible orientated growth. After the 900°C annealing, the number and the intensity of peaks increase, implying a decrease of the amorphous phase and the improvement of the crystallinity of the thin film. For the BTO/Fe_$LaAlO_3$_900°C case, some of its diffraction peaks can be assigned to the most intense peaks of the Ba_2TiO_4 and/or $BaTi_2O_5$ compounds, whereas the remaining and more intense peaks match with some diffraction planes of the three most common iron oxides, implying once again the growth of these phases in a preferential orientation.

The BTO/Fe_MgO_as_dep thin film diffractogram displays several diffraction peaks which can be assigned to a polycrystalline phase of the maghemite and/or magnetite, and to several barium titanate compounds such as Ba_2TiO_4, $BaTi_2O_5$ and/or $BaTi_5O_{11}$. After the 900°C thermal annealing, most of these peaks get sharper and more intense, and there is the emergence of new ones. The new peaks are mostly assigned to the polycrystalline tetragonal phase of $BaTiO_3$ whose emergence is due to the crystallization of its amorphous phase and the decreasing amount of other BTO stoichiometries whose peaks either disappeared or at least got much smaller.

In BTO/Fe_Al2O3_900°C, there are some sharp diffraction peaks which are mainly assigned to the α and γ phases of Fe_2O_3, and to the $BaTi_2O_5$ and $BaTi_5O_{11}$ compounds.

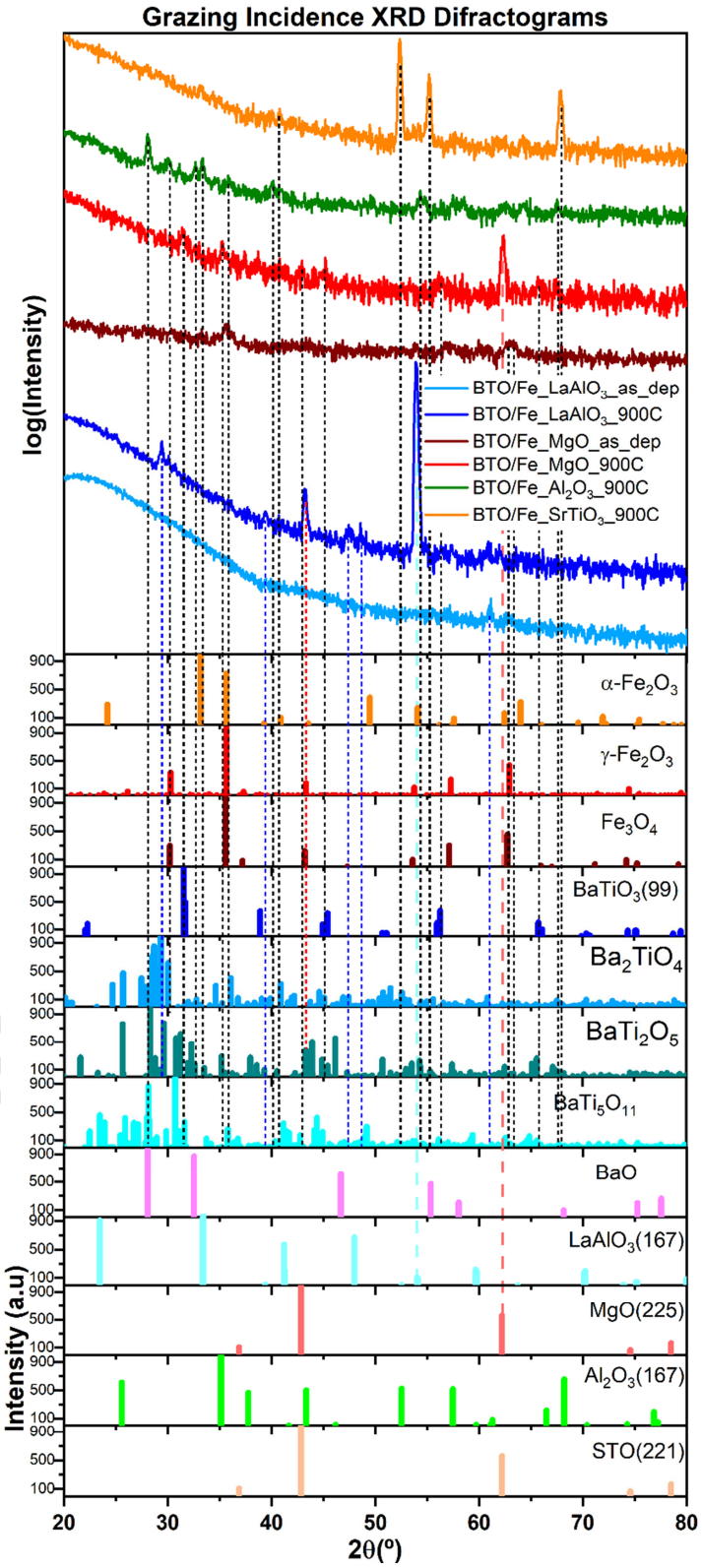

Figure 2: Diffractograms of the BTO/Fe thin films studied in this manuscript and standard diffractograms of possibly relevant phases. The dashed lines correspond to peaks which are aligned with peaks from the standard diffractograms.

The STO substrate structure belongs to the 221 point group and possesses lattice parameters which are identical to the BTO cubic (221) and tetragonal (99) phases, thus the lack of the peaks is related to the growth of the thin films in preferential orientations, mainly for the BTO compounds [27]. Still, there are 3 peaks which are quite sharp and intense at $2\theta \approx 52°$, 55° and 68°. None of these three peaks coincide with any of the substrate diffraction planes, nor with the most intense diffraction planes of any of the phases suggested by the *High Score Plus* phase indexing software. As a matter of fact, these peaks did solely match a very restricted amount of diffraction peaks such as the (220) and (311) diffraction planes of the BaO(225) and some of the low intensity peaks of the Ba_2TiO_4, $BaTi_2O_5$ and $BaTi_5O_{11}$ compounds. The remaining smaller and less well-defined diffraction peaks are compatible to a randomly oriented polycrystalline growth of Ba2TiO4 and $BaTi_2O_5$ phases, and there is the matching of some of its peaks with the (113), (024) and (300) diffraction planes of hematite.

3.2. Raman Spectroscopy Results

Raman spectroscopy is a very sensitive technique which enables the vibrational study of a sample without requiring large crystallites [28, 29].

The incident radiation was a 432nm laser which has a photon energy of about 2.87 eV, close to the 3.2 eV gap energy of BTO [30], thus it is possible to work in a resonance Raman spectroscopy regime, as long as there is some BTO in the thin films. The band gap of hematite and maghemite is about 2.2 eV [31, 32] and 2.0 eV [33], respectively, enabling resonance Raman spectroscopy as well.

Figures 3 and 4 present the Raman spectra for the BTO/Fe thin films deposited on the different substrates, as well as the spectrum of their respective substrate. All the Raman spectra are normalized to the maximum value of each spectrum and the offset of each curve was artificially introduced to ease the presentation of each sample spectrum.

The BTO/Fe LaAlO3 samples clearly have the most prominent Raman modes around 220, 250, 290, 340, 400, 505, 610, 660, 710 and 1400 cm^{-1} matching almost perfectly with the most intense Raman modes of the α-Fe_2O_3 (hematite) and γ-Fe_2O_3 (maghemite) [34-37], presented in table 3 and explicitly assigned in figure 3. For the BTO/Fe_$LaAlO_3$_900°C in particular, there are 3 additional modes which appear near the 305, 520 and 725 cm^{-1} which are assigned to the most intense BaTiO3 Raman modes [29, 38, 39]. This feature suggests that the thermal annealing was enough to enhance the crystallinity/formation of $BaTiO_3$. The shoulder around 800 cm^{-1} is an

indicator of amorphous phases of Ba-Ti-O systems, and/or other barium titanate stoichiometries such as Ba_2TiO_4 and $BaTi_2O_5$, whose small contribution does not allow the individual distinction of these compounds spectra [40-43].

Table 3: Active Raman modes for the main iron oxides. The vw, w, s and vs stand for very weak, weak, strong and very strong respectively.

α-Fe_2O_3 (cm^{-1})		**γ-Fe_2O_3 (cm^{-1})**	**Fe_3O_4 (cm^{-1})**
226 (s)	659 (vs)	350 (w)	193 (vw)
245 (s)	817 (vw)	500 (w)	306 (vw)
292 (w)	1049 (vw)	700 (w)	538 (w)
299 (w)	1103 (vw)	**Fe_2TiO_4 (cm^{-1})**	668 (s)
411 (vs)	1320 (2LO overtone)	495 (s)	**$FeTiO_3$ (cm^{-1})**
497 (w)	1525 (two magnon	561 (w)	≈ 230 (s)
612 (s)	Scattering)	679 (vs)	680 (vs)

Even though figure 3 shows that the same iron oxide phases are present in each of the BTO/Fe_$LaAlO_3$_as_dep and BTO/Fe_$LaAlO_3$_900°C spectra, their relative intensities are clearly different, which implies that the percentage of each iron oxide changes considerably depending on the deposition and annealing conditions. The annealing transforms a portion of the maghemite into its most stable phase, thus the higher percentage of hematite in the BTO/Fe_$LaAlO_3$_900°C spectra Raman spectrum. Moreover, each mode's frequency can also suffer shifts in its energy due to crystal effects, namely the size of the iron oxide particles and/or strain effects [44].

In the Raman spectra, for the depositions made on the MgO substrate, there is a new phase assigned to Fe_3O_4 (magnetite), which is solely present in the "as deposited" thin film. It is also possible to see that after the 900°C thermal annealing, which according to the literature is within the optimal annealing temperature range to increase the crystallinity of BTO thin films [45], there is a clear increase of the BaTiO3 phase and the decrease of the shoulder around 800 cm^{-1} which was associated with the amorphous phase of other BTO stoichiometries. However, at this annealing temperature the magnetite Raman modes disappeared, and there is also a decrease and broadening of the maghemite and hematite Raman modes while the maximum around 700 cm^{-1} increases substantially. The processes involving the iron oxides can be explained by the phase diagram calculated by Ketteler et al. [46], where the annealings at room pressure will promote the formation of a Fe2O3 phase, thus explaining the disappearance of the magnetite phase.

Figure 4 shows that BTO/Fe_Al_2O_3_900°C has quite perceptible Raman modes, in addition to the ones belonging to the substrate. These are related to the presence of hematite as its majority phase, as well as some traces of the maghemite vibrational modes.

On the other hand, for the STO substrate, which has a band gap energy of 3.25 eV [47], there is resonant Raman scattering within the substrate. Therefore, the Raman contribution of the STO substrate completely overshadows any contribution of the thin films, which have an interaction volume several orders of magnitude smaller than the substrate. This problem was not evident for the remaining substrates once they have band gaps > 6 eV, much higher than the photon energy of the incident laser line.

For all the thin films here presented, it is crucial to mention the broad mode around 1400 cm^{-1} assigned to the hematite phase. In fact, this maximum corresponds to two Raman modes: one phonon overtone of a Raman inactive vibrational mode (660 cm^{-1}) at around 1320 cm^{-1} and a mode corresponding to a two magnon Raman scattering which occurs around 1525 cm^{-1} [48-50]. While the overtone remains proximately in the same vibrational energy, the two magnon mode can suffer a shift in energy depending on the overall magnetic and structural properties of the hematite particles deposited on the considered substrates under the different conditions [44]. For the particular case of the BTO/Fe_MgO thin films, after the 900°C thermal annealing there is a greater decrease in the relative intensity of the right part of the high energy maximum (correspondent to the two magnon scattering mode) than in its left part (corresponding to the phonon overtone), thus suggesting a change in the magnetic behaviour of these thin films due to the thermal annealing at room temperature. This change of magnetic properties is supported by the M(T) curves later presented in

figure 10.

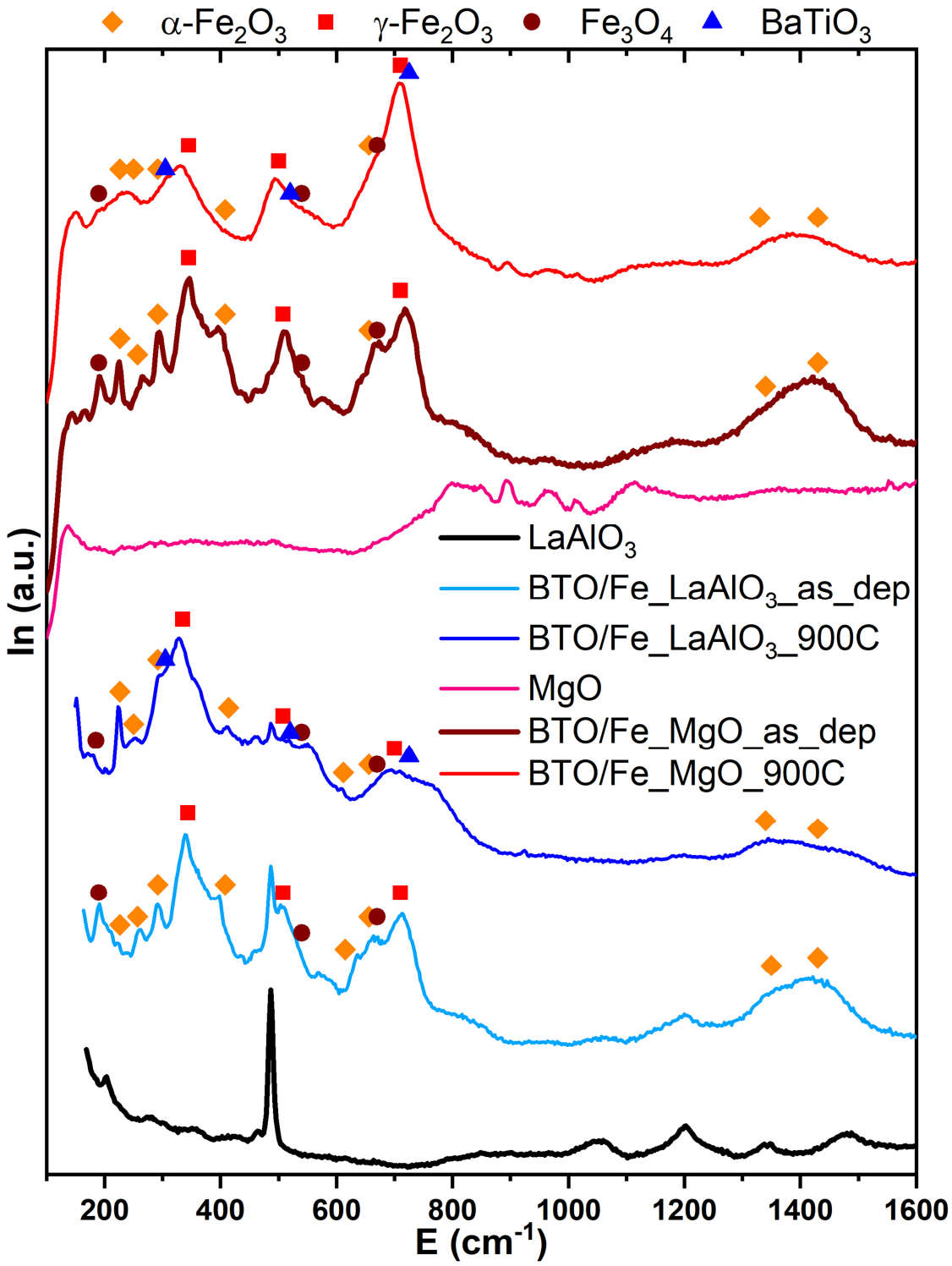

Figure 3: Raman spectra for the BTO/Fe thin films deposited on $LaAlO_3$ and MgO substrates. The substrates' spectra are also presented.

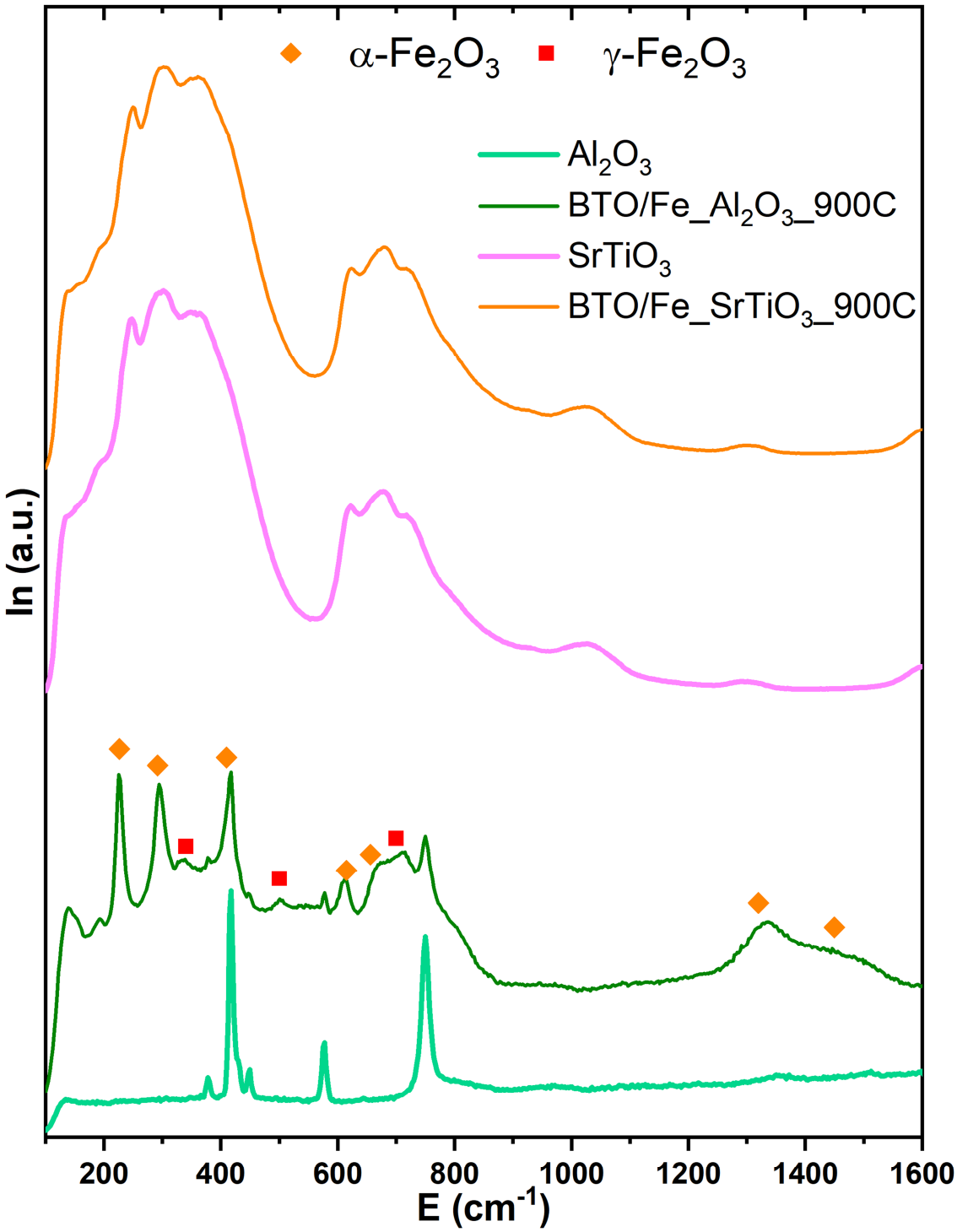

Figure 4: Raman spectra for the BTO/Fe thin films deposited on Al_2O_3 and $SrTiO_3$ substrates. The substrates' spectra are also presented.

3.3. TEM-EDS analysis

To have further morphological and chemical information about the BTO/Fe heterostructures deposited on the MgO substrate, a combined approach of TEM and EDS was performed on the BTO/Fe_MgO_as_dep and BTO/Fe_MgO_900°C thin films.

Figure 5 presents a STEM micrograph of the BTO/Fe_MgO_as_dep thin film. One can observe some thickness fluctuations, with a total thickness of approximately 72 nm.

Once the micrograph contrast does not discriminate the BTO layers from the Fe layers (due to their similar atomic numbers), a TEM-EDS analysis was also performed using an electron beam spot with a FWHM of about 2.5 nm, to confirm the elemental distribution through the deposited film. Figure 6 shows three Fe peaks, with $w \approx 12$nm each, between four Ba/Ti peaks, showing a well-defined separation between the BTO and Fe layers, apart from a small overlap of the Fe and Ba/Ti contributions at the interfaces. The BTO layers are characterized by the Ti and Ba K and L lines, respectively, and the Fe by its K lines. Figure 6 also shows the presence of O through all the BTO/Fe_MgO_as_dep film, confirming the diffusion of O into the Fe layers, thus inducing the latter's oxidation, in good agreement with the GIXRD and Raman results, which show the presence of iron oxides instead of metallic iron.

To evaluate the thermal annealing effects on the deposited thin film, TEM was also performed on the BTO/Fe_MgO_900°C sample. The STEM micrograph presented in figure 7 shows about the same order of thickness and its respective fluctuations, however, the 900°C annealing also induced the diffusion of some film's atoms into the substrate. Figure 7 shows that the diffused atoms can penetrate as deep as 39 nm.

To determine if the BTO and Fe layers were still in a multilayer arrangement, TEM-EDS analysis was again performed using the same beam spot size. As shown in figure 8, the three Fe peaks found on the "as deposited" sample merged into a single broad distribution implying the presence of Fe through all the film volume. A similar feature is also seen for the Ba/Ti case. The O atoms remain in a distribution similar to the "as deposited" one.

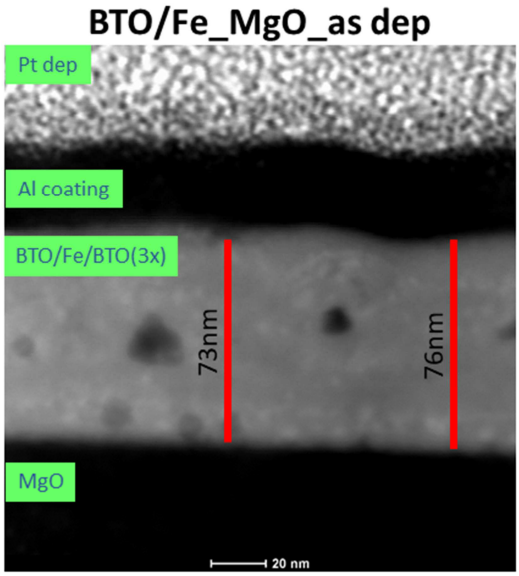

Figure 5: BTO/Fe_MgO_as_dep STEM micrograph

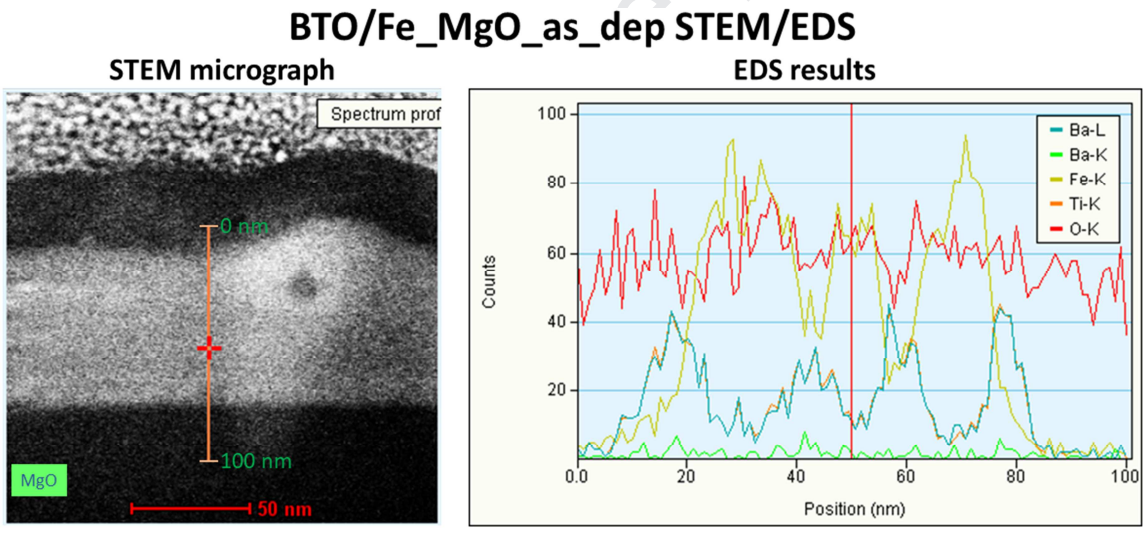

Figure 6: BTO/Fe_MgO_as_dep EDS results from the line specified in the STEM micrograph.

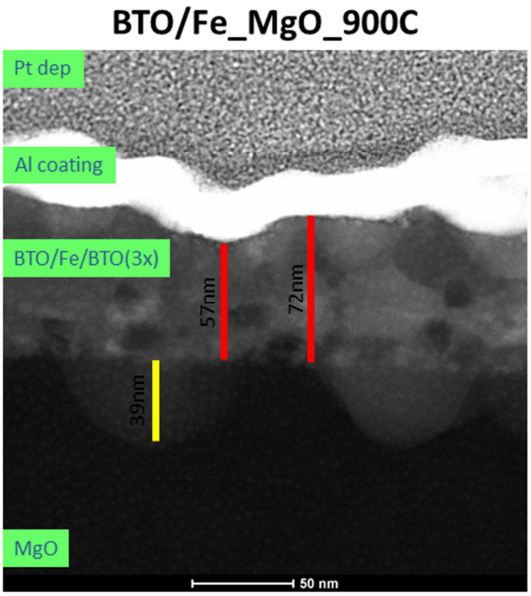

Figure 7: BTO/Fe_MgO_900°C STEM micrograph

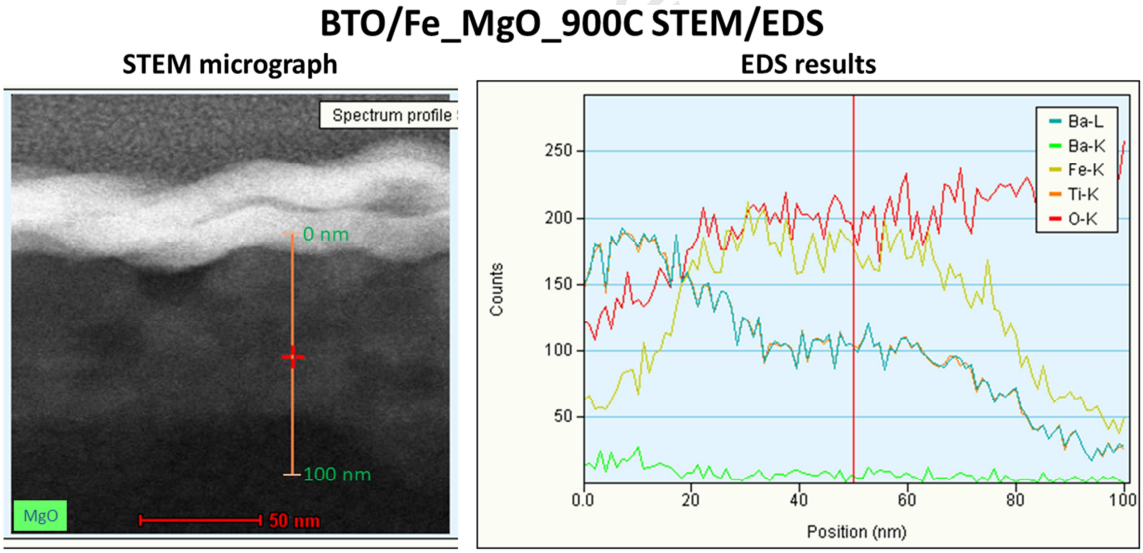

Figure 8: BTO/Fe_MgO_900°C EDS results from the line specified in the STEM micrograph.

3.4. Magnetic Properties

To check if the magnetic properties of the thin films were sensitive to the BTO ferroelectric phase transitions (cubic-tetragonal, tetragonal-orthorhombic, and orthorhombic-rhombohedral), temperature dependent magnetization studies were carried out. Figures 9 to 12 show that, even though the four thin films were deposited simultaneously, they present different magnetic behaviours, before and after the thermal annealings.

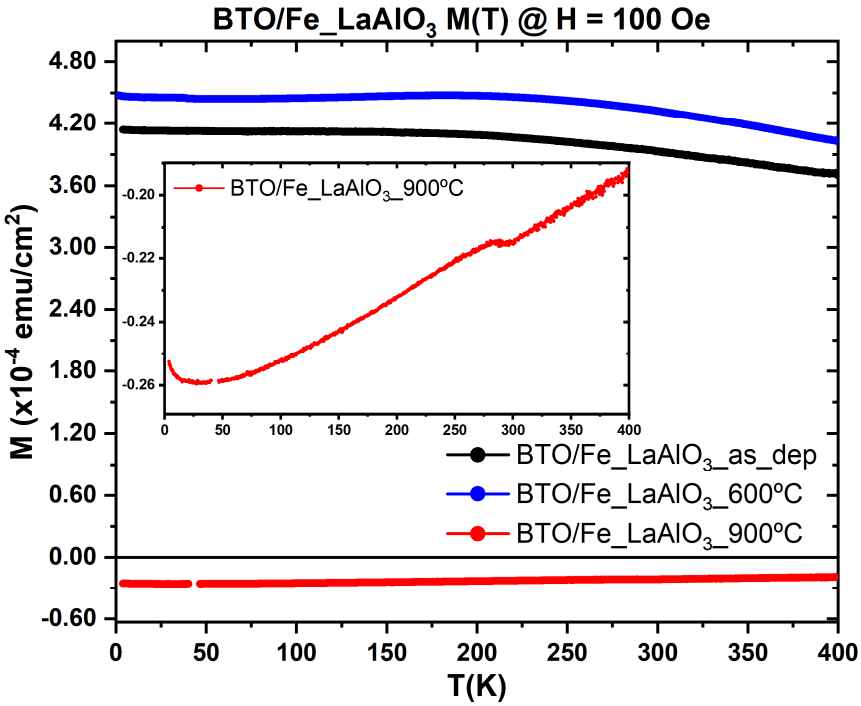

Figure 9: M(T) curves of the BTO/Fe_LaAlO$_3$ thin film for different thermal annealings. The inset of this figure presents a zoom of the BTO/Fe_LaAlO$_3$900°C magnetization.

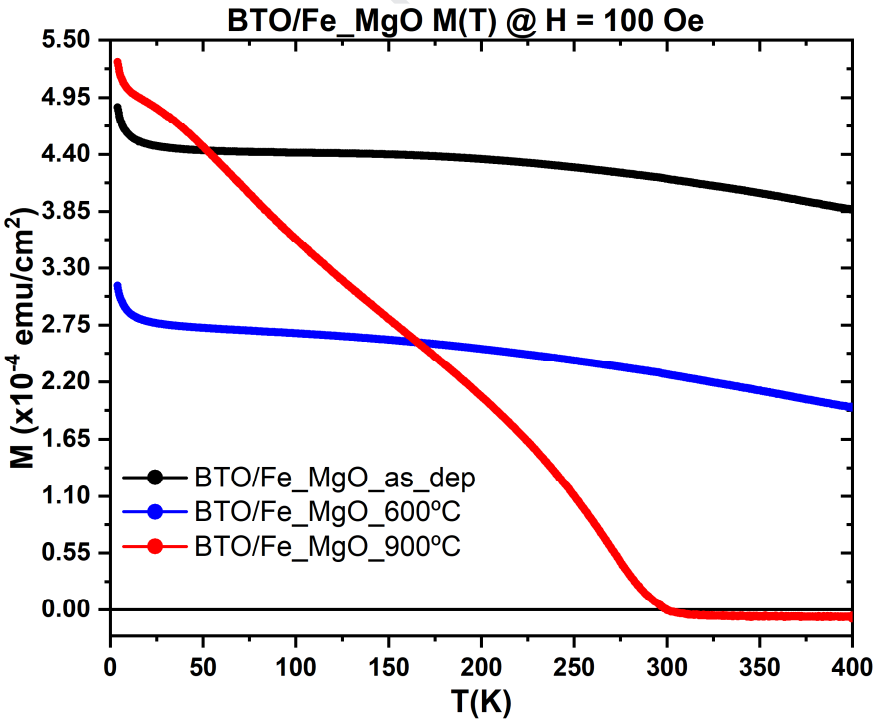

Figure 10: M(T) curves of the BTO/Fe_MgO thin film for different thermal annealings. The low temperature upturn is due to impurities present in the substrate.

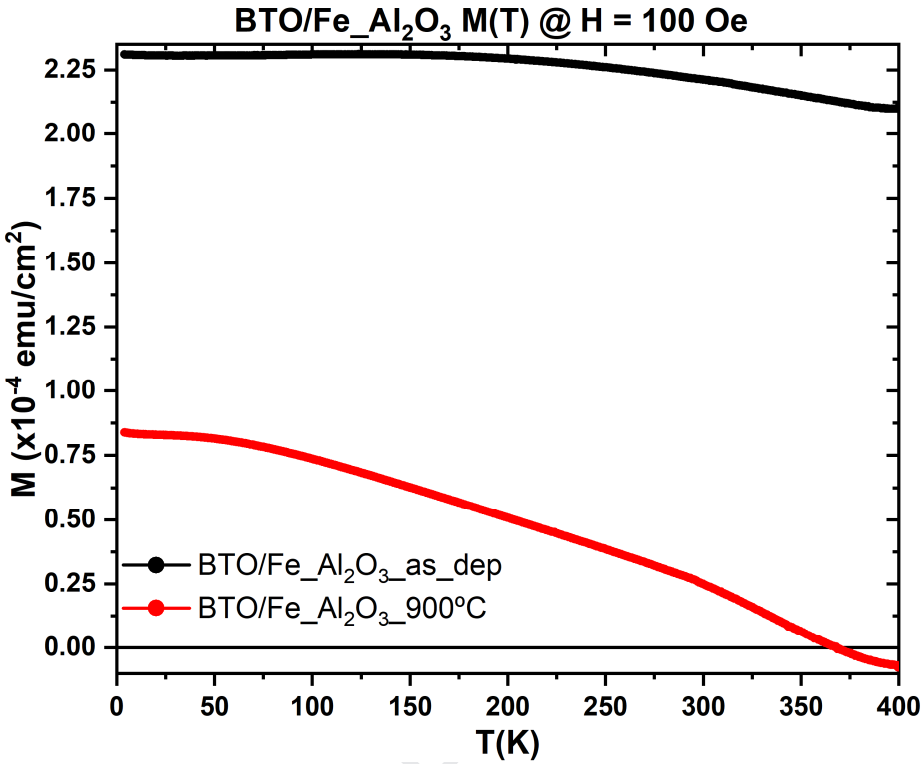

Figure 11: M(T) curves of the BTO/Fe_Al_2O_3 thin film for different thermal annealings.

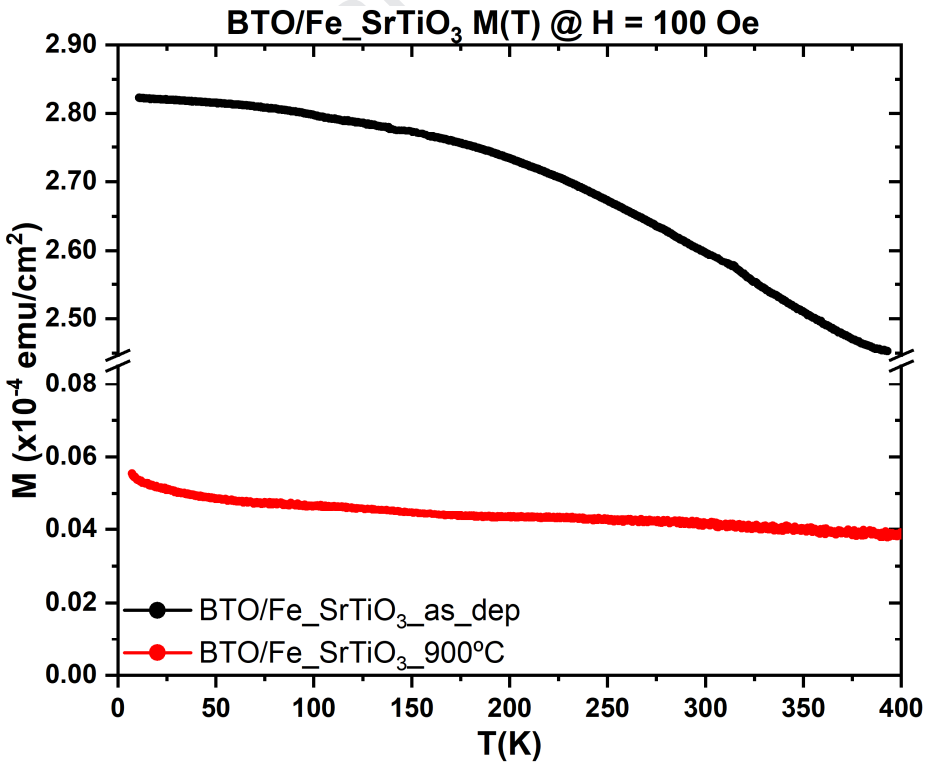

Figure 12: M(T) curves of the BTO/Fe_$SrTiO_3$ thin film for different thermal annealings.

The M(T) curves of all the "as deposited" samples show the presence of an ordered magnetic behaviour with a high T_C (well above the maximum measured temperature, 400 K). Such a feature is not only compatible with Curie temperature of the phase of Fe metal (T_C = 1043 K) but also with the Néel temperatures of the most common iron oxides: α-Fe_2O_3 (T_N = 956 K), γ-Fe_2O_3 (T_N = 820-986 K) and Fe_3O_4 (T_N = 850 K) [51]. This fact is quite important since, as shown by the TEM-EDS analysis, the Fe is apparently in an oxidized form (before and after the thermal annealings). Figure 10 also shows a paramagnetic like upturn curvature at low temperatures (T≤20 K), which results from paramagnetic impurities present in the MgO substrate.

We studied the magnetic properties of each pristine substrate and observed that the paramagnetic contribution is almost negligible for the remaining substrates, when comparing to their intrinsic diamagnetic behaviour, but for the MgO case the paramagnetic contribution overweights the diamagnetic one at low temperatures. This is reported by some suppliers, which mention Fe impurities with concentrations as high as 50 ppm, compatible with the 80 ppm estimated by our magnetic measurements [52].

The annealing at 600°C did not alter qualitatively the magnetization curves of BTO/Fe_$LaAlO_3$ (figure 9) and BTO/Fe_MgO (figure 10), apart from a small vertical shift associated with a change in the saturation magnetization.

On the other hand, at the 900°C annealing, different magnetic behaviours are observed at each substrate (figures 9 to 12). These differences imply that the substrates constrain their thin film into very unalike magnetic phases. The BTO/Fe_$LaAlO_3$_900°C thin film shows a considerable decrease of its magnetization at H=100 Oe, making more evident its diamagnetic behaviour (hence the negative value) and a very small portion of vestigial paramagnetic impurities at low temperatures. Another noteworthy feature is the anomaly around 270K, quite close to the orthorhombic tetragonal BTO phase transition.

The BTO/Fe_MgO_900°C thin film, has a much smaller magnetization at higher temperatures with a strong increase around 270 K, once again suspiciously close to the BTO O T phase transition (figure 10). This temperature has the features of a magnetic transition, separating the paramagnetic and diamagnetic behaviours from a magnetic ordered phase.

The BTO/Fe_$Al_3O_3$900°C thin film (figure 11) presents an overall reduction of its magnetization absolute value at H=100 Oe, as well as a strong decrease above $T_C \approx$ 375 K, close to the BTO T C phase transition.

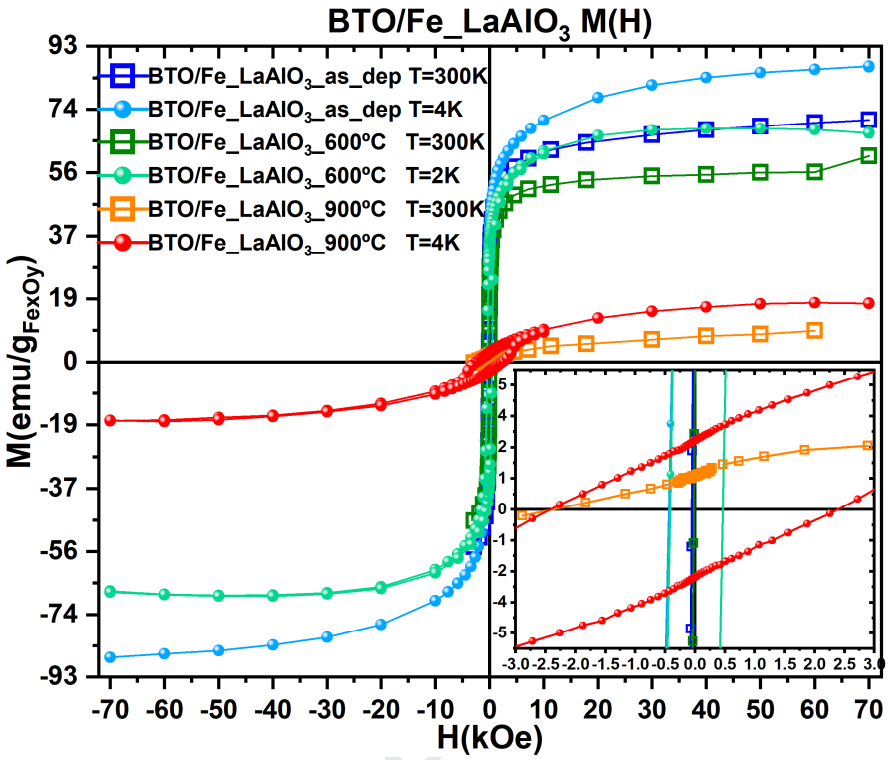

Figure 13: M(H) curves of BTO/Fe_LaAlO$_3$ thin films after removing the substrate's diamagnetic contribution.

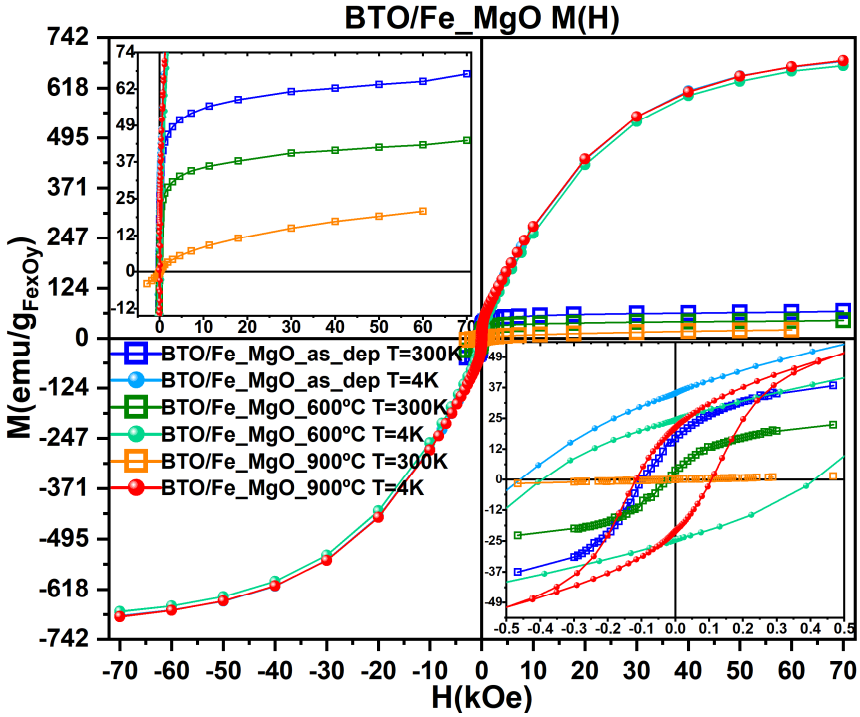

Figure 14: M(H) curves of BTO/Fe_MgO thin films after removing the substrate's diamagnetic contribution. The high values of the magnetization normalized to the iron oxide mass are due to the presence of paramagnetic impurities in the MgO substrate, which for the lower temperature curves are not negligible.

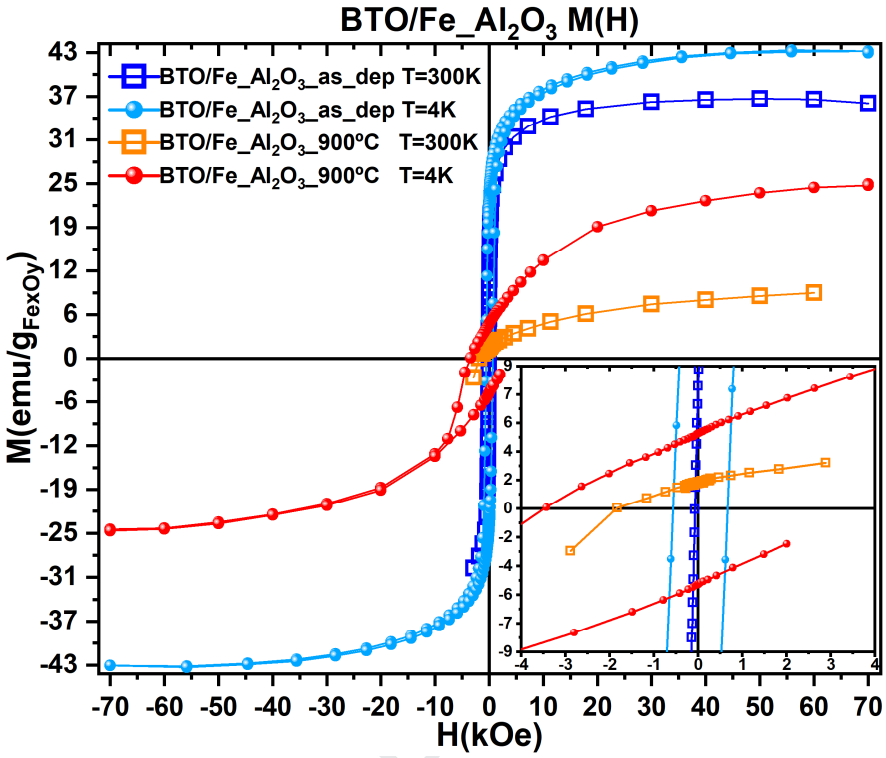

Figure 15: M(H) curves of BTO/Fe_Al_2O_3 thin films after removing the substrate's diamagnetic contribution.

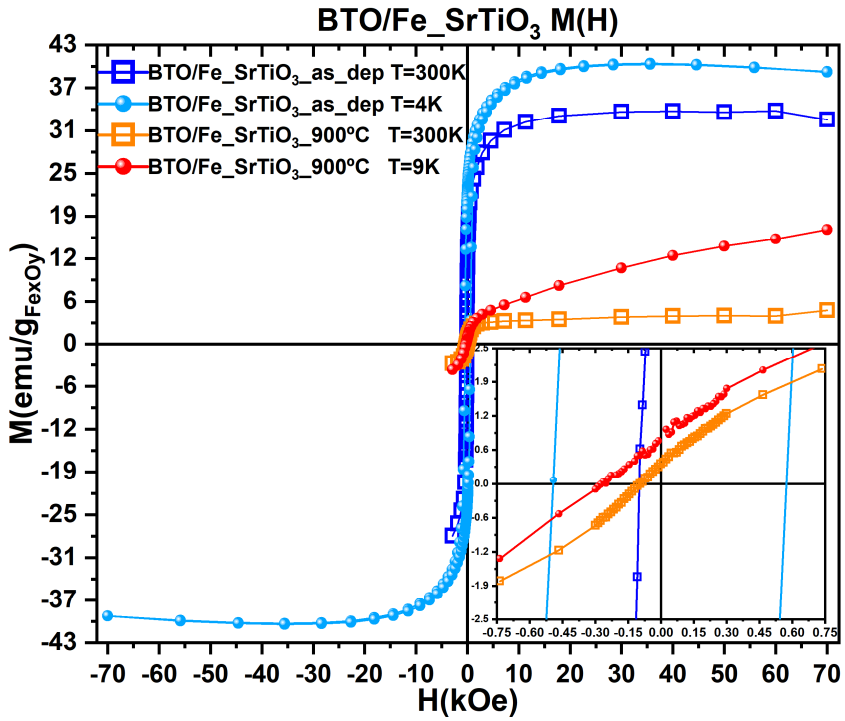

Figure 16: M(H) curves of BTO/Fe_$SrTiO_3$ thin films after removing the substrate's diamagnetic contribution.

A similar effect also occurs for BTO/Fe_$SrTiO_3$_900°C thin film (figure 12), however in this case, besides the decrease in the absolute value of its magnetization at H=100 Oe, there is a fattening of the M(T) curvature, implying either an increase of the TC or a change in its overall magnetic behaviour.

The field dependence of the magnetization was also studied for the four samples at 300K and lower temperatures (typically 4 K), as shown in figures 13 to 16. The presented M(H) curves were obtained after the removal of each substrate's diamagnetic component, which was determined by the M(H) slope at high temperature (usually at 400 K) and for magnetic fields close to 70 kOe. As stated before, the Fe present in the thin films is in an oxidized form, hence, to ease the comparison and analysis of the M(H) curves, the magnetization is presented in emu/g_{FexOy}.

This Fe_xO_y oxide was though as a mixture of the hematite, maghemite and magnetite Fe oxides with an a priori unknown proportion. This normalization was done considering the expected amount of Fe on each thin film (estimated considering a total thickness of 72 nm, based on the STEM micrographs, and assuming the geometry of figure 1), and the arithmetic mean of the hematite, maghemite and magnetite densities. Since their densities are 5.271, 5.074 and 5.197 g/cm^3, respectively [53], assuming the arithmetic mean of these densities, there would always be a < 3% deviation from the real magnetization value (the one that there would be if we knew the correct Fe oxide).

To help the analysis of the M(H) curves, their coercive fields, H_c, and saturation magnetizations, M_s, are presented in table 4. Each presented H_c value is the corrected value after considering the coercive field of the superconductor coil, intrinsic to the magnetometer measurements and whose value is ≈ 23 Oe for measurements which reach a 70 kOe magneticeld. The M_s values were estimated for the ordered part of the M(H) to avoid the inclusion of the paramagnetic component of the substrate impurities (which are particularly high for the MgO substrate).

The symbiosis of the magnetometry, GIXRD, Raman spectroscopy and TEM-EDS results allow an in-depth insight of the physical phenomena present in the BTO/Fe thin films deposited on the four different substrates and the modifications made by the thermal annealings. The saturation magnetizations, M_s, and the magnetic coercive fields, H_C, presented in figures 13 to 16 and table 4 are particularly good physical quantities to distinguish between the mentioned iron oxides. Table 4 summarizes the M_s and H_C quantities obtained by the careful inspection of the magnetization curves

of figures 13 to 16. For the films on MgO, the contribution of the substrate impurities was removed during the estimation of the M_s of the heterostructures.

It is possible to conclude that for all the "as deposited" thin films, the oxidized iron-rich layers consist of a mixture of α-Fe2O3 (M_s = 0.5 emu/g [53]) and γ-Fe2O3 (M_s = 75 emu/g [53]). The proportion of both clearly depends on the substrate where the deposition occurred, as it perceptible from the observation of the Raman results and the saturation magnetization values.

The values of coercive fields measured at 4 and 300K show the presence of qualitatively the same magnetic phases (values in the same order of magnitude, ranging from 460-590 Oe at 4K and 80-120 Oe at 300 K) for the "as deposited" thin films, in spite of some quantitative deviations which corroborate the effects of the substrates on the overall thin film growth.

Table 4: Saturation magnetization, M_s, and coercive field, H_C, estimated for each deposited thin film and respective thermal annealled counterpart.

Sample	M_s (emu/g_{FexOy})	H_C (Oe)	
		LT (4K)	RT (300K)
BTO/Fe_$LaAlO_3$_as_dep	68	459	78
BTO/Fe_$LaAlO_3$_600°C	55	440 (2K)	44
BTO/Fe_$LaAlO_3$_900°C	2.6	2446	2400
BTO/Fe_MgO_as_dep	61	483	120
BTO/Fe_MgO_600°C	40	417	45
BTO/Fe_MgO_900°C	25	140	20
BTO/Fe_Al_2O_3_as_dep	37	592	95
BTO/Fe_Al_2O_3_900°C	4.9	3505	1876
BTO/Fe_$SrTiO_3$_as_dep	34	517	122
BTO/Fe_ $SrTiO_3$_900°C	4.1	296 (9K)	118

The EDS results also support this interpretation, since the BTO/Fe layers remain well defined and separated, while showing a ubiquitous presence of O atoms through the film (figure 6). The thin film deposited on MgO also presents Fe_3O_4 (M_s = 92 emu/g [53]) which is not evident in any other thin film, reinforcing the role of the substrate on the growth of the thin film.

After the 600°C thermal annealing, there is a decrease in all presented saturation magnetizations suggesting a decrease of the maghemite phase (and/or magnetite phase in the particular case of the BTO/Fe_MgO_600°C) in relation to the hematite and/or an increase of the

magnetic disorder of these magnetic oxides. The fact that the measured coercive fields remain in the same order of magnitude before and after the mentioned thermal annealing, apart from small changes in the H_c which may originate from different grain sizes and/or internal stresses of the iron oxides' grains [54-56], is also an evidence that the same iron oxides are present before and after this annealing.

However, after the 900°C thermal annealing there is inter-diffusion of the BTO/Fe layers into a single layer containing partial or total formation of $Fe_xBa_yTi_wO_z$ oxides, thus, the presence of titanohematites and titanomagnetites is quite likely. Nevertheless, the Raman spectra of the titanohematites and titanomagnetites are quite similar to the spectra of the hematite and magnetite combined with the spectra of the ilmenite ($FeTiO_3$) and ulvospinel (Fe_2TiO_4) respectively [57, 58]. Therefore, for Raman spectra such as the ones presented in figures 3 and 4, it might be diffcult to distinguish between the different possible stoichiometries of these compound oxides. Similarly, the XRD peaks of the titanohematites and titanomagnetites occur at about the same places of their pure iron oxides (the deviations in 2θ are much less than the width of our peaks), having simply different relative intensities [59-62]. This will not alter the conclusions since we do not have enough diffraction peaks to enable a comparison between relative intensities.

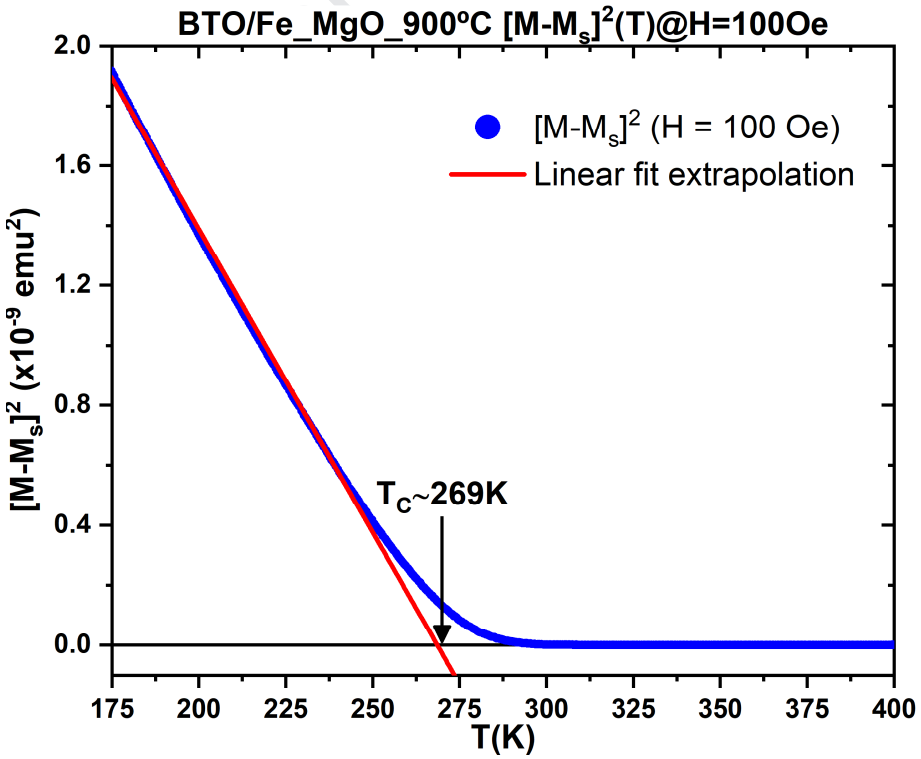

Figure 17: $[M\text{-}M_s]^2$ of BTO/Fe_MgO_900°C as a function of temperature. Using a mean field model linear fit extrapolation, a T_C = 269K is estimated.

Focusing on the BTO/Fe_MgO_900°C, where a magnetic phase transition apparently occurs at ≈ 270 K, the Raman results suggest the presence of titanohematite iron oxides. To have a more accurate estimation of the measured Curie temperature, a spontaneous magnetization mean field model was used, where $M\text{-}M_s/(T_C\text{-}T)^{1/2}$. The magnetization of figure 10 was represented as $[M\text{-}Ms]^2$ versus T (figure 17), using a $M_s \approx M(400K)$, and the linear part of the curve was fitted, resulting in a more accurate value of T_C = 269 K.

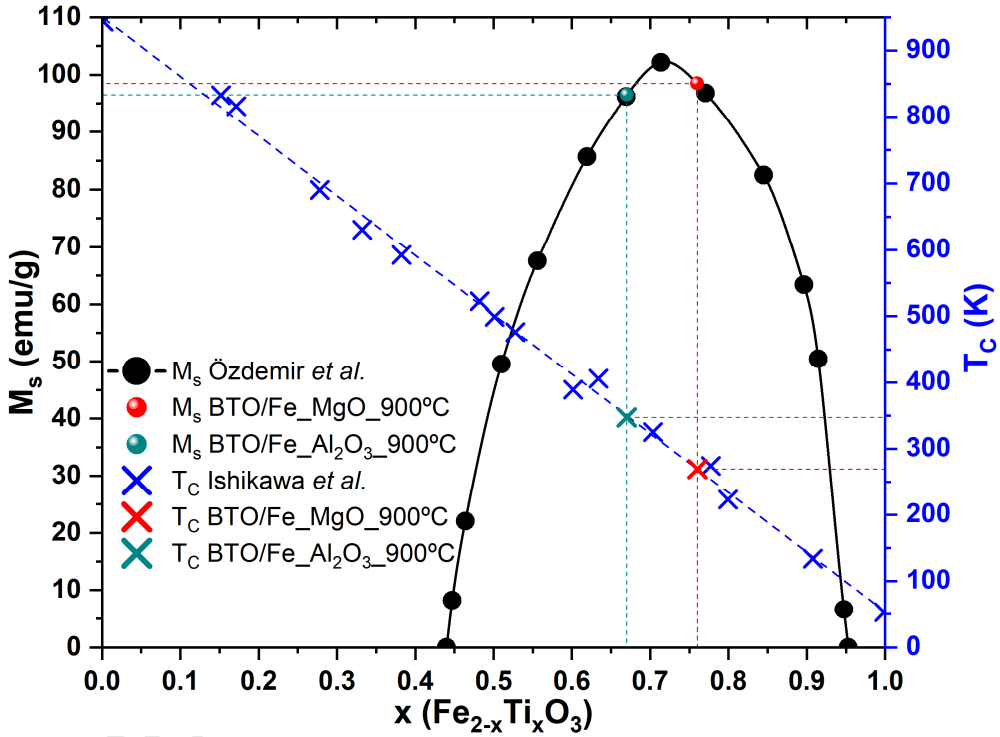

Figure 18: Curie temperatures and saturation magnetization for the Hematite-Ilmenite diagram. Adapted from [53] and [63].

As mentioned, the inter-diffusion of the BTO and Fe layers might lead to a $Fe_xBa_yTi_wO_z$ compound. That could justify the measured magnetization curves and TC. Figure 18 presents two diagrams with the T_C and M_s for the $Fe_{2-x}Ti_xO_3$ system [63], showing that for a stoichiometry close to $Fe_{1.24}Ti_{0.76}O_3$ the T_C occurs at ≈ 269K and M_s ≈ 99 emu/g.

Knowing this, we can justify simultaneously the measured T_C and $M_s \approx 25$ emu/g_{FexOy} assuming a mixture (neglecting magnetic disorder) of 25% $Fe_{1.24}Ti_{0.76}O_3$ and 75% of any other iron oxides with a high T_C and M_s close to the hematite's value (which is found for most stoichiometries of titanomagnetites and titanohematites [64-66]). Moreover, Carmichael shows that in one of the two possible paths of the solvus curvature for the ilmenite-hematite solid solution series, the annealing at 900°C coincides with the temperature needed to get the $Fe_{1.24}Ti_{0.76}O_3$ [67]. Furthermore,

the presence of $Fe_{1.24}Ti_{0.76}O_3$ also justifies the substantial increase of the Raman mode at ≈ 700 cm^{-1} which matches with the strongest mode of $FeTiO_3$ [68].

A similar approach can be used to justify the presence of the faint anomaly close to 375K which occurs for the BTO/Fe_Al_2O_3_900°C. In this case, using spontaneous magnetization models, a T_C ≈ 347K was estimated, which corresponds to a $Fe_{1.33}Ti_{0.67}O_3$ titanohematite with Ms ≈ 97 emu/g. In this particular case, there is also a considerable enhancement of the coercive field when compared with the "as deposited" thin film (table 4), which can be explained by the partial presence of a Barium hexaferrite [69], BaFe12O19. The presence of this oxide is compatible with the Raman spectra of figure 4, since its strongest Raman mode appears just before the 700 cm^{-1} maghemite Raman mode [70], and with an oriented growth of this phase assigned in its diffractogram (figure 2).

The BTO/Fe_$LaAlO_3$_900°C presents a similar behaviour to the BTO/Fe_Al_2O_3_900°C thin film (namely regarding the substantial coercivity increase), yet in the latter case there isn't a magnetic anomaly at ≈ 350K thus, apart from a quite faint anomaly close to 270 K, the majority phase of this thin film should be assigned to a hematite like oxide such as the titanohematites with low value of *x* shown in figure 18 [71]. BTO/Fe_$SrTiO_3$_900°C, on the other hand, seems to have a similar behavior to its "as deposited" and 600°C annealing counterparts, but now with a clearly dominant hematite like, similarly to BTO/Fe_$LaAlO_3$_900°C, but with much lower coercive fields and therefore without the segregation of the Barium hexaferrite phase.

4. Conclusions

In summary, we simultaneously deposited BTO/Fe heterostructures (four 7-15nm BTO layers and three 12nm Fe layers) on $LaAlO_3$, MgO, Al_2O_3 and $SrTiO_3$ substrates using rf-sputtering at low temperature (350°C). We show that the "as deposited" thin films grow in separate BTO/Fe layers, however oxidation of the Fe layers occurs across all their depth.

We found out that each substrate clearly constrains the formation of the Fe layers into different fractions of α-Fe_2O_3, γ-Fe_2O_3 and Fe_3O_4 oxides, despite the simultaneous deposition. These iron oxides magnetic properties do not show any magnetic anomalies around the BTO phase transitions.

To enhance the BTO crystallinity and the magnetic coupling to BTO phase transitions, different annealings were performed at 600°C and 900°C. The magnetic properties show that there are no relevant changes after the 600°C annealings. After the 900°C annealing, TEM-EDS results

show that a substantial ion migration occurs, destroying the multi-layered geometry/nature of the thin films resulting in BTO inclusions within a single heterogeneous blend made from the BTO and Fe layers. We found the formation of specific titanohematite oxides ($Fe_{2-x}Ti_xO_3$) and BTO like compounds, whose stoichiometries are constrained by the substrate.

In the BTO/Fe_$LaAlO_3$_900°C and BTO/Fe_$SrTiO_3$_900°C thin films there is the formation of $Fe_{2-x}Ti_xO_3$ compounds with $x \leq 0.4$, presenting hematite like magnetic properties. On the other hand, the BTO/Fe_MgO_900°C and BTO/Fe_Al_2O_3_900°C thin films present the formation of $Fe_{1.24}Ti_{0.76}O_3$ and $Fe_{1.33}Ti_{0.67}O_3$, as identified by the $T_C \approx 269K$ and 347 K, respectively. These two titanohematites have quite competitive magnetic properties, when compared with other typical ferrites, with $M_s \approx 99$ emu/g and $M_s \approx 97$ emu/g, respectively.

Altogether, we show that the choice of a proper substrate for the deposition of BTO/Fe heterostructures can be used as a way to tune the desired magnetic properties of the resultant thin film, given convenient deposition and annealing conditions. This study also points out the inherent complexity and uncountable ways of working with BTO/Fe heterostructures, which are yet to be completely understood to be used as an appealing accessible high performance magnetoelectric material [72].

5. Acknowledgements

This work was developed within the scope of the project CICECO-Aveiro Institute of Materials, POCI-01-0145-FEDER-007679 (FCT Ref. UID /CTM/50011/2013), financed by national funds through the FCT/MEC and when appropriate co-financed by FEDER under the PT2020 Partnership Agreement. FCT is also acknowledged for the grant SFRH/BD/93336/2013 (C.O. Amorim). M R Correia acknowledges FCT Portuguese Foundation for Science and Technology under the projects UID/CTM/50025/2019.

References

[1] S. W. Cheong, M. Mostovoy, Multiferroics: a magnetic twist for ferroelectricity, Nature materials 6 (1) (2007) 13-20.

[2] M. Fiebig, T. Lottermoser, D. Meier, M. Trassin, The evolution of multiferroics, Nature Reviews Materials 1 (8) (2016) 16046.

[3] S. Dong, J. M. Liu, S. W. Cheong, Z. Ren, Multiferroic materials and magnetoelectric physics: symmetry, entanglement, excitation, and topology, Advances in Physics 64 (5-6) (2015) 519-626.

[4] C. A. Vaz, Electric Field control of magnetism in multiferroic heterostructures, Journal of Physics: Condensed Matter 24 (33) (2012) 333201.

[5] J. Scott, Data storage: Multiferroic memories, Nature materials 6 (4) (2007) 256-257.

[6] J. Ma, J. Hu, Z. Li, C. W. Nan, Recent progress in multiferroic magnetoelectric composites: from bulk to thin films, Advanced Materials 23 (9) (2011) 1062-1087.

[7] J. Zhai, Z. Xing, S. Dong, J. Li, D. Viehland, Detection of pico-tesla magnetic fields using magneto-electric sensors at room temperature, Applied physics letters 88 (6) (2006) 062510.

[8] W. G.Wang, M. Li, S. Hageman, C. Chien, Electric-Field-assisted switching in magnetic tunnel junctions, Nature materials 11 (1) (2012) 64.

[9] G. Srinivasan, I. Zavislyak, A. Tatarenko, Millimeter-wave magnetoelectric effects in bilayers of barium hexaferrite and lead zirconate titanate, Applied physics letters 89 (15) (2006) 152508.

[10] J. Y. Son, J. H. Lee, S. Song, Y. H. Shin, H. M. Jang, Four-states multiferroic memory embodied using Mn-doped $BaTiO_3$ nanorods, ACS nano 7 (6) (2013) 5522-5529.

[11] N. Spaldin, R. Ramesh, Advances in magnetoelectric multiferroics, Nature materials 18 (3) (2019) 203.

[12] N. A. Hill, Why are there so few magnetic ferroelectrics?, The Journal of Physical Chemistry B 104 (29) (2000) 6694-6709.

[13] C. Song, B. Cui, F. Li, X. Zhou, F. Pan, Recent progress in voltage control of magnetism: Materials, mechanisms, and performance, Progress in Materials Science 87 (2017) 33-82.

[14] J. M. Hu, L. Q. Chen, C. W. Nan, Multiferroic heterostructures integrating ferroelectric and magnetic materials, Advanced Materials 28 (1) (2016) 15-39.

[15] F. Matsukura, Y. Tokura, H. Ohno, Control of magnetism by electric fields, Nature nanotechnology 10 (3) (2015) 209.

[16] C. Israel, N. Mathur, J. Scott, A one-cent room-temperature magnetoelectric sensor, Nature materials 7 (2) (2008) 93.

[17] W. Eerenstein, M. Wiora, J. Prieto, J. Scott, N. Mathur, Giant sharp and persistent converse magnetoelectric effects in multiferroic epitaxial heterostructures, Nature materials 6 (5) (2007) 348.

[18] M. Liu, O. Obi, J. Lou, Y. Chen, Z. Cai, S. Stoute, M. Espanol, M. Lew, X. Situ, K. S. Ziemer, V. G. Harris, N. X. Sun, Giant electric field tuning of magnetic properties in multiferroic ferrite/ferroelectric heterostructures, Advanced Functional Materials 19 (11) (2009) 1826-1831.

[19] S. Zhang, Y. G. Zhao, P. S. Li, J. J. Yang, S. Rizwan, J. X. Zhang, J. Seidel, T. L. Qu, Y. J. Yang, Z. L. Luo, Q. He, T. Zou, Q. P. Chen, J. W. Wang, L. F. Yang, Y. Sun, Y. Z. Wu, X. Xiao, X. F. Jin, J. Huang, C. Gao, X. F. Han, R. Ramesh, Electric-Field control of nonvolatile magnetization in $Co_{40}Fe_{40}$ B_{20}/Pb $(Mg_{1/3}Nb_{2/3})_{0.7}Ti_{0.3}O_3$ structure at room temperature, Physical review letters 108 (13) (2012) 137203.

[20] R. Cheri, V. Ivanovskaya, L. Phillips, A. Zobelli, I. Infante, E. Jacquet, V. Garcia, S. Fusil, P. Briddon, N. Guiblin, A. Mougin, A. A. Unal, F. Kronast, S. Valencia, B. Dkhil, A. Barthélémy, M. Bibes, Electric-Field control of magnetic order above room temperature, Nature materials 13 (4) (2014) 345.

[21] C. Amorim, F. Figueiras, J. Amaral, P. M. Vaghefi, P. Tavares, M. Correia, A. Baghizadeh, E. Alves, J. Rocha, V. Amaral, Peculiar magnetoelectric coupling in $BaTiO_3$: Fe_{113ppm} nanoscopic segregations, ACS applied materials & interfaces 7 (44) (2015) 24741-24747.

[22] F. Figueiras, C. Amorim, J. Amaral, J. A. Moreira, P. Tavares, E. Alves, V. Amaral, Magnetoelectric effect probe through ppm Fe doping in $BaTiO_3$, Journal of Alloys and Compounds 661 (2016) 495-500.

[23] K. J. L. Company, Barium titanate (BaTiO3) sputtering targets, [Online; accessed 14-June-2018] (1996-2018). URL https://www.lesker.com/newweb/deposition_materials/depositionmaterials_sputtertargets_1.cfm?pgid=ba3

[24] C. GmbH, CrysTec GmbH Data-Sheets, [Online; accessed 14-June-2018] (2018).URL http://www.crystec.de/datasheets-e.html

[25] A. C. L. S. Marques, Advanced Si pad detector development and Sr-TiO_3 studies by emission channeling and hyperfine interaction experiments, (PhD Thesis) (2009).

[26] J. W. Jang, S. J. Chung, W. J. Cho, T. S. Hahn, S. S. Choi, Thickness dependence of room temperature permittivity of polycrystalline $BaTiO_3$ thin films by radio-frequency magnetron sputtering, Journal of applied physics 81 (9) (1997) 6322-6327.

[27] W. Zhang, M. Yuan, X. Wang, W. Pan, C. M. Wang, J. Ouyang, Design and preparation of stress-free epitaxial $BaTiO_3$ polydomain films by rf magnetron sputtering, Science and technology of advanced materials 13 (3) (2012) 035006.

[28] M. H. Frey, D. A. Payne, Grain-size effect on structure and phase transformations for barium titanate, Physical Review B 54 (5) (1996) 3158.

[29] M. El Marssi, F. Le Marrec, I. Lukyanchuk, M. Karkut, Ferroelectric transition in an epitaxial barium titanate thin film: Raman spectroscopy and x-ray diffraction study, Journal of applied physics 94 (5) (2003) 3307-3312.

[30] K. Suzuki, K. Kijima, Optical band gap of barium titanate nanoparticles prepared by rf-plasma chemical vapor deposition, Japanese journal of applied physics 44 (4R) (2005) 2081.

[31] B. Gilbert, C. Frandsen, E. R. Maxey, D. M. Sherman, Band-gap measurements of bulk and nanoscale hematite by soft x-ray spectroscopy, Physical Review B 79 (3) (2009) 035108.

[32] A. J. Deotale, R. Nandedkar, Correlation between particle size, strain and band gap of iron oxide nanoparticles, Materials Today: Proceedings 3 (6) (2016) 2069-2076.

[33] M. I. Litter, M. A. Blesa, Photodissolution of iron oxides. IV. A comparative study on the photodissolution of hematite, magnetite, and maghemite in EDTA media, Canadian Journal of Chemistry 70 (9) (1992) 2502-2510.

[34] M. Lübbe, A. M. Gigler, R. W. Stark, W. Moritz, Identification of iron oxide phases in thin films grown on Al_2O_3 (0001) by Raman spectroscopy and x-ray diffraction, Surface Science 604 (7-8) (2010) 679-685.

[35] D. De Faria, S. Venâncio Silva, M. De Oliveira, Raman microspectroscopy of some iron oxides and oxyhydroxides, Journal of Raman spectroscopy 28 (11) (1997) 873-878.

[36] S. J. Oh, D. Cook, H. Townsend, Characterization of iron oxides commonly formed as corrosion products on steel, Hyperfine interactions 112 (1-4) (1998) 59-66.

[37] I. Chamritski, G. Burns, Infrared-and Raman-active phonons of magnetite, maghemite, and hematite: a computer simulation and spectroscopic study, The Journal of Physical Chemistry B 109 (11) (2005) 4965-4968.

[38] P. K. Dutta, P. Gallagher, J. Twu, Raman spectroscopic study of the formation of barium titanate from an oxalate precursor, Chemistry of materials 5 (12) (1993) 1739-1743.

[39] C. Perry, D. Hall, Temperature dependence of the Raman spectrum of $BaTiO_3$, Physical Review Letters 15 (17) (1965) 700.

[40] J. Javadpour, N. G. Eror, Raman spectroscopy of higher titanate phases in the $BaTiO_3$-TiO_2 system, Journal of the American Ceramic Society 71 (4) (1988) 206-213.

[41] L. Preda, L. Courselle, B. Despax, J. Bandet, A. Ianculescu, Structural characteristics of rf-sputtered $BaTiO_3$ thin films, Thin Solid Films 389 (1-2) (2001) 43-50.

[42] M. Rössel, H. R. Höche, H. Leipner, D. Völtzke, H. P. Abicht, O. Hollricher, J. Müller, S. Gablenz, Raman microscopic investigations of $BaTiO_3$ precursors with core-shell structure, Analytical and bioanalytical chemistry 380 (1) (2004) 157-162.

[43] L. H. Robins, D. L. Kaiser, L. D. Rotter, P. K. Schenck, G. T. Stauf, D. Rytz, Investigation of the structure of barium titanate thin films by Raman spectroscopy, Journal of applied physics 76 (11) (1994) 7487-7498.

[44] F. J. Owens, J. Orosz, Effect of nanosizing on lattice and magnon modes of hematite, Solid state communications 138 (2) (2006) 95-98.

[45] J. Olson, D. Stevison, I. Bransky, The effect of temperature on properties of rf sputtered $BaTiO_3$ films, Ferroelectrics 37 (1) (1981) 685-686.

[46] G. Ketteler, W. Weiss, W. Ranke, R. Schl ogl, Bulk and surface phases of iron oxides in an oxygen and water atmosphere at low pressure, Physical Chemistry Chemical Physics 3 (6) (2001) 1114-1122.

[47] K. Van Benthem, C. Elsässer, R. French, Bulk electronic structure of $SrTiO_3$: experiment and theory, Journal of applied physics 90 (12) (2001) 6156-6164.

[48] K. McCarty, Inelastic light scattering in α-Fe_2O_3: Phonon vs magnon scattering, Solid State Communications 68 (8) (1988) 799-802.

[49] T. Martin, R. Merlin, D. Human, M. Cardona, Resonant two magnon Raman scattering in α-Fe_2O_3, Solid State Communications 22 (9) (1977) 565-567.

[50] M. J. Massey, U. Baier, R. Merlin, W. H. Weber, Effects of pressure and isotopic substitution on the Raman spectrum of α-Fe_2O_3: identification of two-magnon scattering, Physical Review B 41 (11) (1990) 7822.

[51] R. Cornelle, U. Schwertmann, The iron oxides. Wiley-VCH GmbH & Co, KGa. A.

[52] I. Sigma-Aldrich, Magnesium oxide (single crystal substrate), [Online;accessed 14-June-2018] (2018). URL https://www.sigmaaldrich.com/catalog/product/aldrich/634700?lang=pt&region=PT

[53] Ö. Özdemir, D. J. Dunlop, Rock Magnetism (1997).

[54] Ö. Özdemir, D. J. Dunlop, Hysteresis and coercivity of hematite, Journal of Geophysical Research: Solid Earth 119 (4) (2014) 2582-2594.

[55] C. Rath, K. Sahu, S. Kulkarni, S. Anand, S. Date, R. Das, N. Mishra, Microstructure-dependent coercivity in monodispersed hematite particles, Applied Physics Letters 75 (26) (1999) 4171-4173.

[56] H. Itoh, T. Sugimoto, Systematic control of size, shape, structure, and magnetic properties of uniform magnetite and maghemite particles, Journal of colloid and interface science 265 (2) (2003) 283-295.

[57] A. Wang, K. Kuebler, B. Jolli, L. A. Haskin, Mineralogy of a martian meteorite as determined by Raman spectroscopy, Journal of Raman Spectroscopy 35 (6) (2004) 504-514.

[58] M. Bauer, P. Davydovskaya, M. Janko, M. Kaliwoda, N. Petersen, S. Gilder, R. W. Stark, Raman spectroscopy of laser-induced oxidation of titanomagnetites, Journal of Raman Spectroscopy 42 (6) (2011) 1413-1418.

[59] R. J. Harrison, S. A. Redfern, R. I. Smith, In-situ study of the R3 to R3c phase transition in the ilmenite-hematite solid solution using time-of-flight neutron powder diffraction, American Mineralogist 85 (1) (2000) 194-205.

[60] I. K. Sedler, A. Feenstra, T. Peters, An x-ray powder diffraction study of synthetic (Fe, $Mn)_2TiO_4$ spinel, European Journal of Mineralogy (1994) 873-886.

[61] J. P. Wright, A. M. Bell, J. P. Attfield, Variable temperature powder neutron diffraction study of the Verwey transition in magnetite Fe_3O_4, Solid State Sciences 2 (8) (2000) 747-753.

[62] M. Sorescu, L. Diamandescu, D. Tarabasanu Mihaila, V. Teodorescu, B. Howard, Hydrothermal synthesis and structural characterization of (1-x) α-$Fe_2O_{3-x}SnO_2$ nanoparticles, Journal of Physics and Chemistry of Solids 65 (5) (2004) 1021-1029.

[63] Y. Ishikawa, S. i. Akimoto, Magnetic properties of the $FeTiO_3$-Fe_2O_3 solid solution series, Journal of the Physical Society of Japan 12 (10) (1957) 1083-1098.

[64] P. Dankers, Relationship between median destructive field and remanent coercive forces for dispersed natural magnetite, titanomagnetite and hematite, Geophysical Journal International 64 (2) (1981) 447-461

[65] M. Ozima, N. Sakamoto, Magnetic properties of synthesized titanomaghemite, Journal of Geophysical Research 76 (29) (1971) 7035-7046.

[66] D. Krása, J. Matzka, Inversion of titanomaghemite in oceanic basalt during heating, Physics of the Earth and Planetary Interiors 160 (2) (2007) 169-179.

[67] C. Carmichael, The magnetic properties of ilmenite-hematite crystals, Proc. R. Soc. Lond. A 263 (1315) (1961) 508-530.

[68] X. Wu, S. Qin, L. Dubrovinsky, Structural characterization of the $FeTiO_3$-$MnTiO_3$ solid solution, Journal of Solid State Chemistry 183 (10) (2010) 2483-2489.

[69] R. C. Pullar, Hexagonal ferrites: a review of the synthesis, properties and applications of hexaferrite ceramics, Progress in Materials Science 57 (7) (2012) 1191-1334.

[70] J. Kreisel, S. Pignard, H. Vincent, J. Senateur, G. Lucazeau, Raman study of $BaFe_{12}O_{19}$ thin films, Applied physics letters 73 (9) (1998) 1194-1196.

[71] M. Tadic, N. Citakovic, M. Panjan, B. Stanojevic, D. Markovic, Jovanovic, V. Spasojevic, Synthesis, morphology and microstructure of pomegranatelike hematite (α-Fe_2O_3) superstructure with high coercivity, Journal of Alloys and Compounds 543 (2012) 118-124.

[72] C. O. Amorim, J. S. Amaral, J. N. Gonçalves, V. S. Amaral, Electric field induced room temperature null to high spin state switching: A computational prediction, Advanced Theory and Simulations 1900005.

Highlights

- $BaTiO_3$/Fe heterostructures deposited using magnetron sputtering on different substrates
- The substrate constrains the growth of the deposited thin films
- The substrate constrains the ferrite formation after thermal treatment for T≥900°C
- Formation of magnetic competitive titano-ferrites on some of the substrates

Declaration of interests

☒ The authors declare that they have no known competing financial interests or personal relationships that could have appeared to influence the work reported in this paper.

☐The authors declare the following financial interests/personal relationships which may be considered as potential competing interests: